The International Journal of Advanced Manufacturing Technology (2018) 99:2353–2363
https://doi.org/10.1007/s00170-018-2643-0

ORIGINAL ARTICLE

Effect of heat input on phase content, crystalline lattice parameter, and residual strain in wire-feed electron beam additive manufactured 304 stainless steel

Sergei Yu. Tarasov[1] · Andrey V. Filippov[1] · Nikolai L. Savchenko[1] · Sergey V. Fortuna[1] · Valery E. Rubtsov[1] · Evgenii A. Kolubaev[1] · Sergey G. Psakhie[1]

Received: 1 May 2018 / Accepted: 26 August 2018 / Published online: 1 September 2018

Abstract
Structural and mechanical characterization of electron beam additive manufactured stainless steel samples has been carried out. The XRD measured austenite and ferrite lattice parameters showed their sensitivity to the heat input value, which was related to the chromium atom redistribution. The ferrite content depended on the heat input too. Optimal heat input level has been detected, which allowed obtaining the tensile strength higher than that of the base stainless steel. Residual strain levels in the as-deposited metal and fusion line zone have been measured using the X-ray $\sin^2\psi$ method. The highest tensile residual strain was determined in a fusion line zone between the first as-deposited layer and a substrate. The microstructure of the first fusion line zone contained deformation twins and entangled dislocations generated by plastic flow under thermal expansion-contraction cycles.

Keywords Wire-feed electron beam additive manufacturing · Stainless steel · Heat input · Lattice parameter · Twinning

1 Introduction

The majority of papers on additive manufacturing (AM) is dedicated to powder-bed processes, while less quantity of them is focused on the directed energy deposition by either particle blown or wire-feed techniques [1–12]. Even smaller number of papers is focused on the wire-feed electron beam free forming of stainless steel, which is a high deposition rate process used for additive manufacturing of components intended for high-temperature and corrosion-resistant applications [2, 11, 12]. The wire-feed AM process is similar to the multipass welding deposition in distinction to the powder-bed processes. Therefore, all basic metallurgical and solidification processes occurring in the melted pool during the wire-feed AM are similar to those occurring in the multipass welding deposition. Analyzing the literature sources, one can see that not so many papers have been devoted to stainless steels wire-feed AM; therefore, there is lack of information on structural evolution in this steel, which determines the anisotropy of mechanical characteristics. The most part of the data and information known on this topic has been collected in a review [11].

It is known from welding that depending upon the *Cr/Ni* ratio there are two principal crystallization mechanisms, such as primary austenite dendrite (*AF* mode) or primary ferrite dendrite growth (*FA* mode) [12]. Thus, either ferrite or austenite becomes a second crystallizing phase in *AF* or *FA* mode, respectively. Ferrite may crystallize in two forms, namely lacy or vermicular ferrite depending upon the growth direction orientation with respect to the unmelted austenite grains.

The abovementioned solidification routes are modified in the course of additive manufacturing due to multipass as well as layer-by-layer building procedure and inevitable formation of partially melted and reheated zones, where both phase transformation and recrystallization may occur [13]. These zones are clearly seen in additive manufactured stainless steel samples as dark-etched fusion lines, and they determine the anisotropy of mechanical characteristics in the AM built metal. The fusion lines mark zones where both structural modifications occur as well as the residual stresses are concentrated [14].

✉ Sergei Yu. Tarasov
tsy@ispms.ru

[1] Institute of Strength Physics and Materials Science SB RAS, pr. Academicheskii 2/4, Tomsk, Russia

Both structural evolution of the solidified metal structure and residual stress level depend on the temperatures achieved. In fact, the multipass deposition creates conditions for thermal cycling the underlying metal layers [15].

All these phenomena occur during additive manufacturing on the 304 stainless steel. Depending upon the temperatures achieved, the reheated zone metal may experience ferrite dissolution in austenite and then precipitation in some other form. The temperature conditions in the vicinity of a melted pool are determined by a heat input level. Therefore, one may trace the heat input effect on the structure and characteristics of the build-up. Determining the precise austenite and ferrite lattice parameters in the build-up zones and as a function of heat input may help better understanding the alloying atom redistribution during remelting and reheating.

The objective of this paper is to follow the crystalline structure changes in the additive manufactured stainless steel build-up as well as to establish a relationship between these changes and the mechanical characteristics.

2 Materials and methods

Directed electron beam free-form fabrication has been carried out using an experimental electron beam deposition machine and 304 stainless steel 1 mm diameter wire. The AM process parameters are shown below in the Table 1. Total five 1-mm thickness layers have been deposited according to scanning strategies shown in Fig. 1. Thus, sample 1 consisted of five layers successively deposited layers each of them being deposited by changing the pass orientation by 90° with respect to the underlying layer. Samples 2 and 3 were composed five layers deposited successively in parallel to each other.

Substrates were $140 \times 75 \times 10$ mm^3 304 stainless steel plates structurally composed of coarse austenite grains with annealing twins and ferrite streaks. Chemical composition of the steel is as follows: (mass %) 0.12 C, 9.5 Ni, 18.4 Cr, 1.4 Mn, 0.8 Si, balance Fe. The corresponding nickel/chromium equivalent is $Cr_{eq}/Ni_{eq} = 1.42$, which means that primary austenite dendrites will crystallize from the melt followed by the ferrite crystallization in the interdendrite spaces between the austenite dendrites (AF mode).

A microstructural characterization has been carried out on samples ground using an emery paper and then polished using a diamond 60-nm grit paste. An electrochemical etching in 10 vol% oxalic acid in water solution was applied so that the sample was an anode and plate electrodes were cathodes. The etching process voltage, current, and time were as follows: 6.1 V, ~ 0.05 A, and 30–40 s, respectively.

TEM thin foils have been prepared by ion milling using an EM 09100IS machine (Jeol) at 6 and 2 kV after a 4° angle tilt. A Jeol 2100 electron microscope operated at 200 kV was used for conventional bright- and dark-field imaging.

An X-ray diffractometer XRD-7000S operated in the 2Θ range 20 to 165°, using CoKa = 1.78897 A radiation, the Bragg-Brentano focusing geometry, and equipped with a monochromator has been used to determine the crystalline lattice parameters and residual strain. To provide the required accuracy of lattice parameter measuring, we used both symmetrical and asymmetrical grazing angle X-ray diffractometry (XRD) schemes. The residual strain was measured using the $\sin^2\psi$- method.

Samples for mechanical testing have been cut out of the deposited metal as shown in Fig. 2 from three parts of the deposited metal volume. These three parts of samples microstructurally represented the as-deposited AM metal, as-deposited/substrate fusion zone, and substrate base metal, respectively. The samples have been chemically etched by dipping for 6 s into the marble reagent composed of 20 mg Cu_2SO_4, 100 ml HCl, 100 ml ethyl alcohol, and then rinsed/dried in ethyl alcohol at the room temperature. The tensile samples had 3-mm thickness, 8-mm width, and 25-mm gauge length. A tensile machine Testsystems 110 M-10 has been used for testing them at the room temperatures. Fractographic analysis was carried out using an SEM instrument NIKKISO SM3000.

The electron beam wire-feed AM process parameters are identified in Table 1 together with the mechanical characteristics and heat input levels calculated as $E = \frac{60*U*I}{1000*V}$, where U

Table 1 The wire-feed electron beam AM deposition process parameters and mechanical characteristics of the samples built

No of sample and scanning strategy	Current, mA	Voltage, kV	Deposition speed, mm/min	Heat input, kJ/mm	σ_{max}, MPa	σ_y, MPa	Percent elongation, %	Overlap, mm	Wire-feed rate, mm/min
1 (Scheme I)	30	30	200	0.27	534	221	94.7	3.2	965
2 (Scheme II)	33	25	200	0.24	557	280	88.1	3.3	800
2 (Scheme II) 1st layer/substrate)	33	25	200	0.24	492	257	86.5	3.3	800
2 (Substrate)	N/A	N/A	N/A	N/A	539	295	84.3	N/A	N/A
3 (Scheme III)	33	25	220	0.22	534	238	88.0	3.3	865

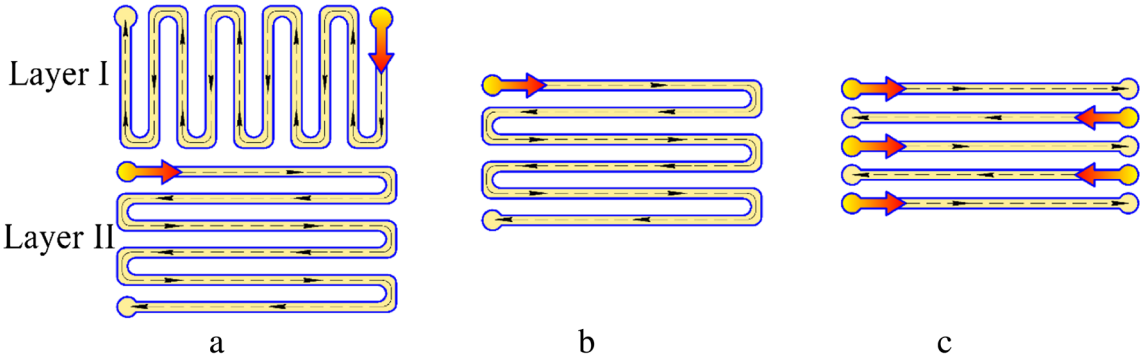

Fig. 1 Scanning strategies used for the wire-feed electron beam manufacturing: Scheme I—successively criss-cross deposited layers (**a**), Scheme II—continuous successive deposition of parallel layers (**b**), Scheme III—linear discontinuous deposition of parallel layers (**c**)

and I are the electron beam voltage and current, V and A, respectively; V is the deposition speed, mm/min.

3 Results

3.1 Metallography

Metallographic examination of the deposited samples allowed showing that the build-up metal of all samples consisted of primary austenite dendrites and thin ferrite crystallites located in spaces between the austenite dendrites (Fig. 3a). The ferrite crystallite morphology varied from vermiculate to cellular, lathy or point-like depending upon the austenite dendrite growth axis orientation with respect to the polished view plain, which was simultaneously parallel to the building direction and the deposition direction. The microstructure of the substrate/build-up fusion zone is depleted by ferrite, which forms coarse cells (Fig. 3b).

3.2 Mechanical strength

The engineering stress-strain curves in Fig. 4 show that both scanning strategy and heat input have their effects on the tensile strength. The sample 1 (0.27 kJ/mm) metal showed the maximum of relative elongation (94.7%) and simultaneously the strength level negligibly below that that of the substrate metal and sample 2 (0.247 kJ/mm) (Fig. 4a). At the same time, sample 2 deposited metal showed its strength higher than that of sample 1 and 3 (0.225 kJ/mm). Also, the deposited on sample 2 metal has the maximum strength as compared to those of metal/substrate transition zone and even the substrate (Fig. 4b).

The as-deposited metal fracture surfaces of sample 1 and sample 3 are composed of ductile fracture dimple structures and < 5-μm cavities (Fig. 5a, c). Sample 1 shows the most irregular surface with ridges and valleys. Sample 3 fracture surface is less irregular as compared to that of sample 1. Sample 2 as-deposited metal shows uniform small flat dimple structures with scarce cavities (Fig. 5b). Sample 2 fusion zone reveals the presence of coarse 20–30 μm cleavage facets similar to those found in a greater number on the fracture surface of the base metal sample (Fig. 6a, b).

3.3 Crystalline lattice parameter

The X-ray irradiated surface was perpendicular to the building direction so that the grown dendrites were inclined to this surface at arbitrary angles. The results of XRD show the presence of two main phases, such as austenite and ferrite both in

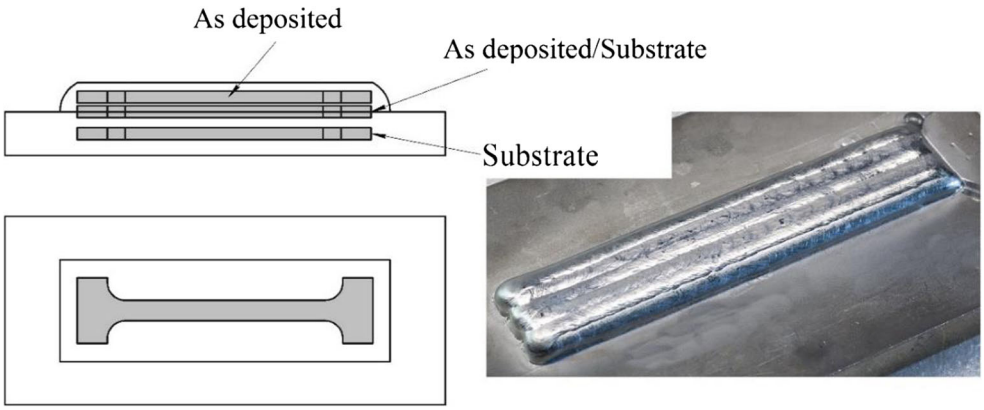

Fig. 2 Tensile test samples cut-off scheme from different parts of the deposited metal

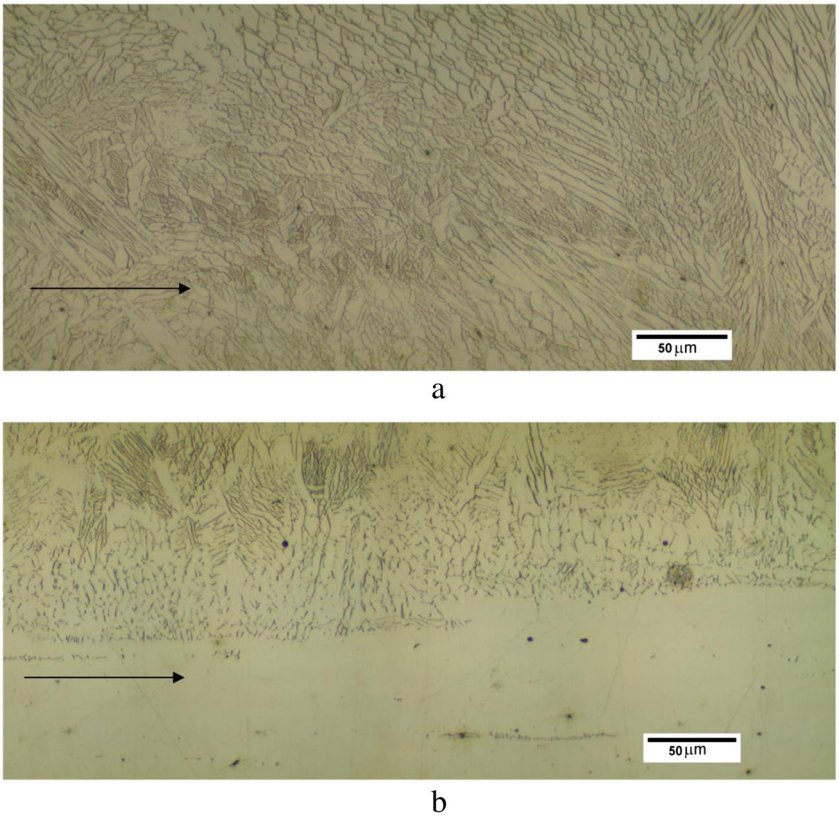

Fig. 3 The microstructure of as-deposited metal (**a**), as-deposited metal/substrate zone (**b**) in samples cut off as shown in Fig. 2. Arrows show the deposition direction

as-deposited metal of all samples (Fig. 7a) and in sample 2 zones (Fig. 7b). One may see that the (200) γ peak is higher than that of (111) γ only in sample 1, which was grown at the maximum heat input 0.27 kJ/mm.

Precision determining the γ-lattice parameters of samples has been carried out using the Nelson-Railey extrapolation function (Fig. 8).

One can see that the extrapolation lines in Fig. 8a give different lattice parameters, for sample, 1, 2, and 3. Let us note that the high data scatter in as-deposited metal might be determined by the presence of lattice defects and an orientation dependence of the residual stresses in the deposited metal. The maximum lattice parameter is inherent to sample 1, the minimum—to sample 2. From Fig. 8b, it can be seen that the substrate has maximum lattice parameter as well as less data scatter from the extrapolation line. The minimum parameter is found for the as-deposited metal.

The effect of heat input on the γ-phase lattice parameter as well as both γ- and δ-phase content measured by the XRD peak ratios is demonstrated by Fig. 9a.

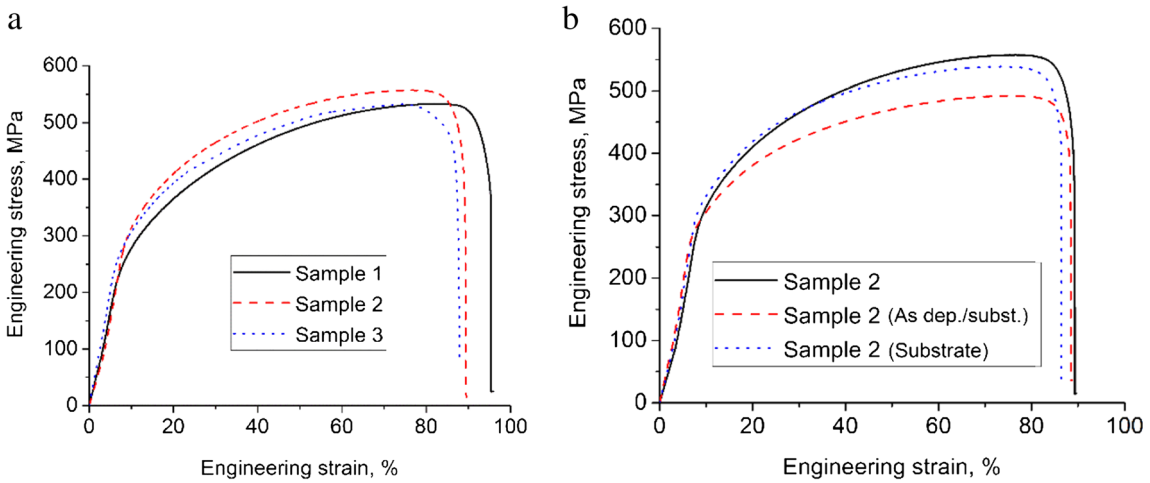

Fig. 4 The engineering stress-strain curves obtained on samples 1, 2, and in tensile axis orientation along the beam travel direction (**a**) and in sample 2 with tensile axis along the building direction (**b**)

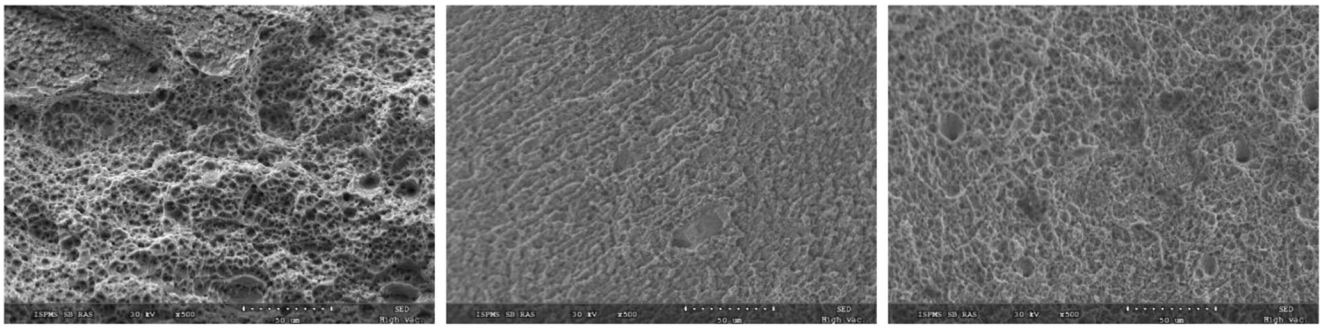

Fig. 5 The SEM images of fracture surfaces on sample 1 (**a**), sample 2 (**b**), and sample 3 (**c**)

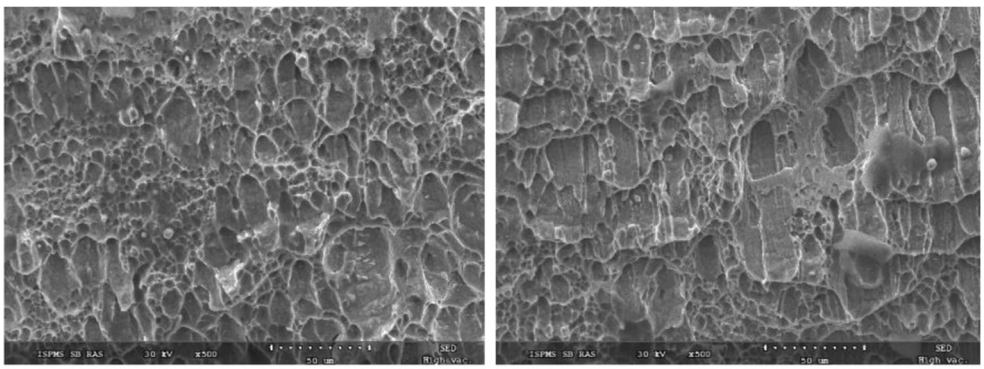

Fig. 6 The SEM images of fracture surfaces in fusion zone (**a**) and base metal (**b**) of sample 2

Both γ-lattice parameter and content reduce with higher heat input until reaching a value of 0.27 kJ/mm when both of them start growing. An inverse behavior is observed for the ferrite whose content grows with the heat input and then starts reducing (Fig. 9b). The ferrite lattice parameter's behavior is analogous to that of austenite (Fig. 9b).

The dependence of ferrite content on the heat input obtained from a quantitative analysis of optical images is in

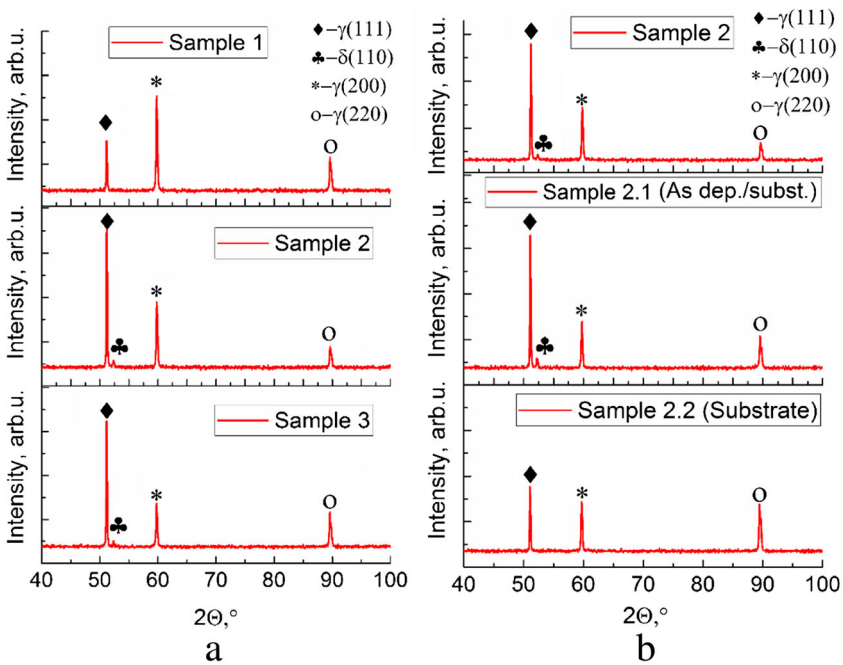

Fig. 7 The XRD patterns obtained from as-deposited metal of samples 1, 2, 3 (**a**) and from sample 2 zones (**b**)

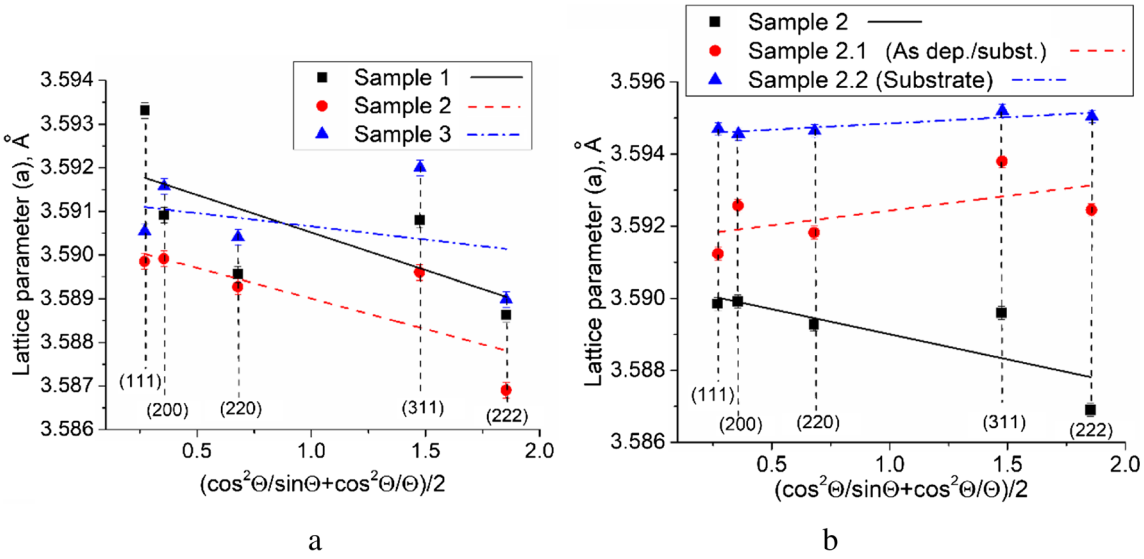

Fig. 8 Extrapolation of austenite lattice parameter using the Nelson-Railey function

accordance with that obtained from XRD (Fig. 10a) but gives somewhat higher ferrite content percentages. The amount of ferrite in different sample 2 zones shows the minimum ferrite content in the as-deposited metal, maximum content for the fusion zone between as-deposited metal and substrate and medium content for the substrate base metal (Fig. 10b).

3.4 Residual strain

Residual strain analysis conducted using the $\sin^2\psi$- method shows low tensile strain ($\Psi = 0°$) levels 0.04% in sample 2 and somewhat higher but still low ones in samples 1 and 3 (up to 0.1%) (Fig. 11a).

It follows from Fig. 11a that the higher heat input resulted in somewhat higher residual tensile strain. It seems quite logical. The distribution of residual stress in sample 2 shows that minimum tensile strain is inherent with the as-deposited metal (Fig. 11b) and the substrate. Up to 20%, tensile strain is observed in the fusion zone between the as-deposited metal and substrate. It follows from the asymmetrical XRD that lattice parameters have wide scatter from the mean value, thus showing both the presence of texturing and orientation dependence of the strain. For example, the lattice parameters determined from (200) reflection show their increased values both due to texture and maximum tensile strain along the (100) dendrite growth axis. Therefore, accurate determination of residual strain and stress as-depended on the orientation was not a purpose in this case.

3.5 TEM

A thin foil for TEM has been cut out of the sample 2 fusion zone, where maximum residual strain has been observed using the XRD. The thin foil surface was parallel to the building direction and tensile axis so that one could see the structural evolution of the samples along the building direction. It was

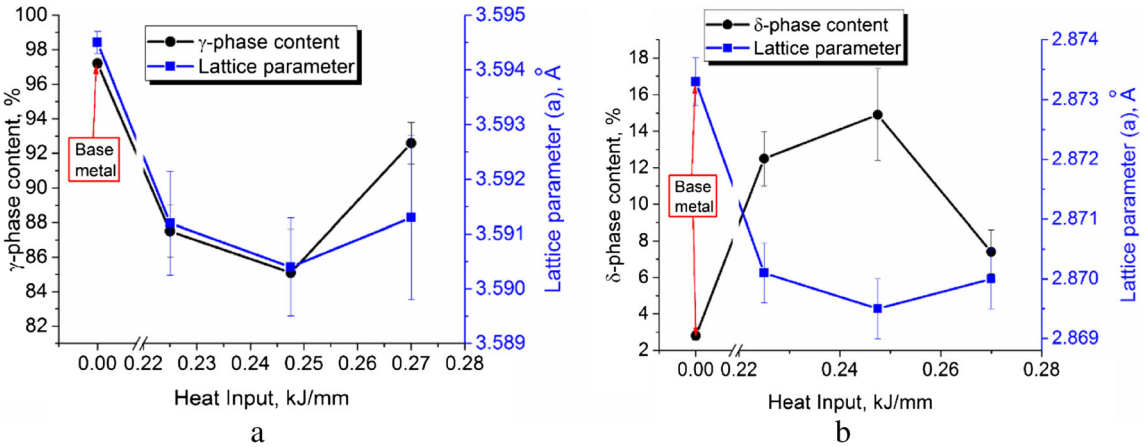

Fig. 9 The heat input effect on the γ-lattice parameter and γ-phase content (**a**) and on δ-phase lattice parameter and content (**b**) in the deposited metal

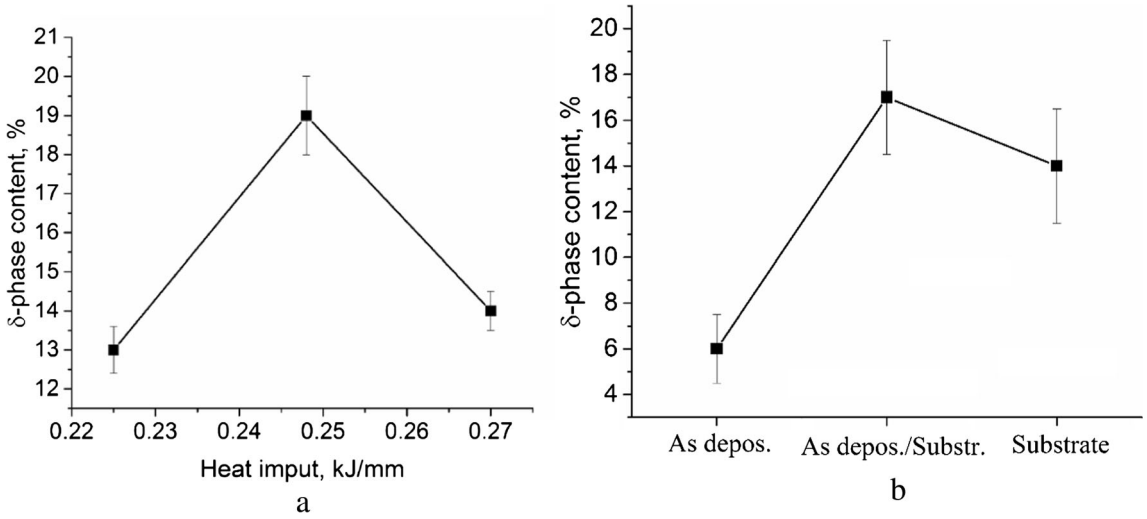

Fig. 10 Ferrite content vs. heat input (**a**) and in different zones of the sample 2 sample (**b**) as determined from optical images using the intercept method

found that this zone was composed of large austenite grains separated one from another by thin ferrite crystallites. The austenite grains belonging to this zone contain thin deformation twins as well as numerous dislocations (Fig. 12a, b). The corresponding SAED area (Fig. 12c) pattern (Fig. 12d) shows the twinning plain $(111)_\gamma$ as a solid line. The dark-field images (Fig. 12e, d) obtained in a twin (e) and matrix (f) reflections identify twins and matrix, respectively. All matrix reflections do not show any azimuthal misorientation.

Ferrite crystallites are located along the austenite grain boundaries and contain less dislocations (Fig. 13a, b). The SAED area (Fig. 13c) and corresponding SAED pattern (Fig. 13d) show the presence of at least two different crystalline lattices. Both phases do not show any azimuthal misorientation. The dark-field images (Fig. 13e, f) were obtained using an austenite and ferrite reflections, respectively. One may see that the ferrite plate in Fig. 13c has been broken into several pieces as a result of thermal expansion-contraction deformation.

4 Discussion

The microstructure of the samples grown using the electron beam multipass deposition is represented by two structural components typical for directed energy deposited 304 stainless steel. The volume content ratio between austenite and ferrite is changed as-depended on the heat input. Such a finding may be explained by the fact that chromium atoms are forced out of the austenite crystalline lattice at the crystallization front into interdendrite spaces during the austenite dendrite growth. The higher heat input accelerates this process,

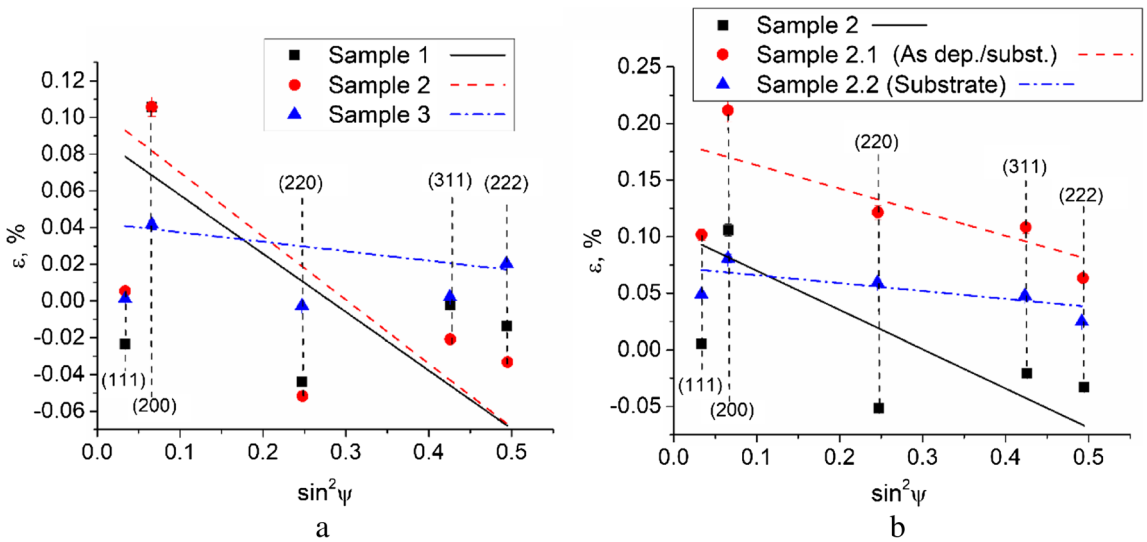

Fig. 11 Residual strain extrapolation as determined from $\sin^2\psi$- method and as dependent on heat input (**a**) and along the building direction ($\Psi = 0°$) (**b**)

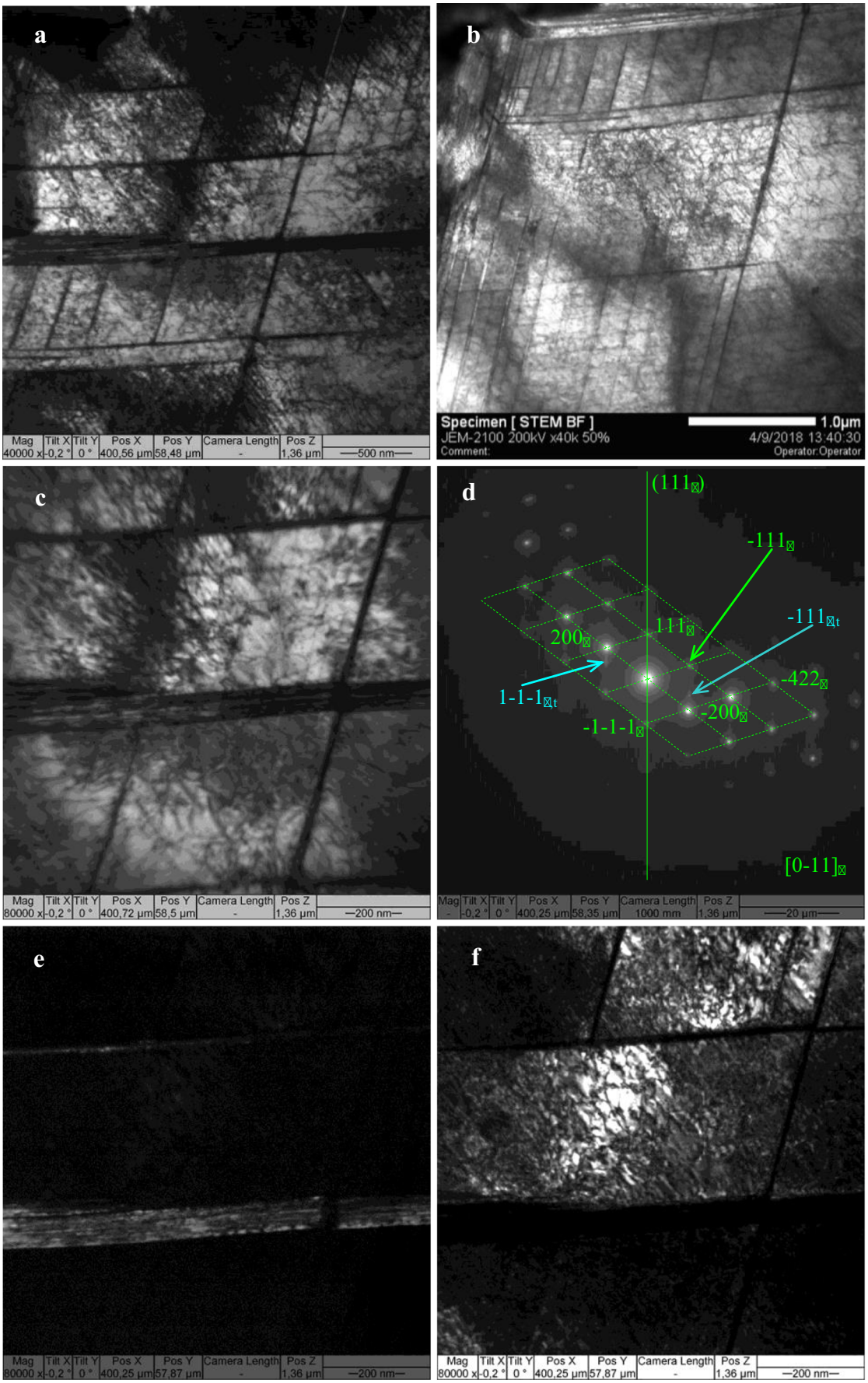
a
Mag 40000 x | Tilt X -0,2 ° | Tilt Y 0 ° | Pos X 400,56 µm | Pos Y 58,48 µm | Camera Length - | Pos Z 1,36 µm | 500 nm
b
Specimen [STEM BF]
JEM-2100 200kV x40k 50%
Comment:
1.0µm
4/9/2018 13:40:30
Operator:Operator
c
Mag 80000 x | Tilt X -0,2 ° | Tilt Y 0 ° | Pos X 400,72 µm | Pos Y 58,5 µm | Camera Length - | Pos Z 1,36 µm | 200 nm
d
(111)
-111
111
-111t
200
-422
1-1-1t
-200
-1-1-1
[0-11]
Mag - | Tilt X -0,2 ° | Tilt Y 0 ° | Pos X 400,25 µm | Pos Y 58,35 µm | Camera Length 1000 mm | Pos Z 1,36 µm | 20 µm
e
Mag 80000 x | Tilt X -0,2 ° | Tilt Y 0 ° | Pos X 400,25 µm | Pos Y 57,87 µm | Camera Length - | Pos Z 1,36 µm | 200 nm
f
Mag 80000 x | Tilt X -0,2 ° | Tilt Y 0 ° | Pos X 400,25 µm | Pos Y 57,87 µm | Camera Length - | Pos Z 1,36 µm | 200 nm

◀ **Fig. 12** TEM bright-field images of deformation twins formed in the as-deposited metal/substrate zone in sample 2 (**a**, **b**, **c**) and corresponding SAED pattern (**d**). Dark-field images have been obtained using a twin reflection $(1\bar{1}\bar{1})_{\gamma,t}$, which is identical to $(5\bar{1}\bar{1})_{\gamma}$ (**e**) and a matrix reflection $(200)_{\gamma}$ (**f**). The austenite and ferrite lattice zone axes are along $[112]_{\gamma}$ and $[111]_{\alpha}$, respectively

thus reducing the austenite lattice parameter and enriching the interdendrite spaces by chromium, which is a ferrite promoting metal. Therefore, increasing the heat input from 0.225 (sample 3) to 0.247 kJ/mm (sample 2) results in increasing the ferrite content and simultaneous reducing the austenite content.

The rationale behind decreasing ferrite lattice parameter in 0.225 to 0.247 kJ/mm range may be as follows. Since ferrite content is increasing in this heat input range then less chromium is left in the austenite; therefore, less of it finds its way to the interdendrite spaces. The solidifying ferrite crystallites are formed in these depleted by chromium interdendrite spaces. Then, already solidified ferrite crystallite will contain less chromium; therefore, their lattice parameter will be decreased as compared to those formed at lower heat input.

Quite another type of behavior is observed in case of increasing the heat input from 0.247 to 0.27 kJ/mm (sample 1). The austenite/ferrite ratio increased as well as austenite and ferrite lattice parameters. It seems that reheating of the deposited metal by successive layer deposition resulted in the ferrite dissolution in austenite. A part of ferrite grains became dissolved and then might partially precipitate again in the form of equiaxed grains. Another part of the chromium atoms stayed dissolved in the austenite, thus increasing its lattice parameter. The same is true for the ferrite since there was no any chromium atom shortage for the ferrite growth by chromium diffusion from austenite during the reheating cycles.

Both new and primary ferrite grains are saturated by chromium; therefore, their lattice parameter increased.

Other researchers confirm the ferrite content growth with the heat input (see for example [16]).

The as-deposited metal of sample 2 is characterized by the maximum content of ferrite as compared to those of sample 1 and 3. Also, sample 2 shows the maximum tensile strength, i.e., higher than that of the base metal. At the same, its yield stress is a bit lower than of the base metal. One may suggest that high ferrite content allowed strengthening the as-deposited metal.

The results of our investigations show that high strength sample 2 as-deposited metal correlates with the heat input and the ferrite content. The fractography results show that fracture surface of as-deposited sample 2 consists of shallow dimples smaller than those in samples 1 and 3.

However, high ferrite content should affect the ductility. Nevertheless, the percent elongation of sample 2 (88%) has not reduced that much as compared to sample 3 (88%) and the base metal (84.3%). The maximum elongation of sample 1 (94.7%) with the maximum heat input what may be explained by less ferrite content as well as defect annealing. Therefore, the high strength and yield stress of sample 2 cannot be fully related to the higher content of ferrite in it. One may suggest that the austenite dendrite size was smaller too and higher strength of sample 2 may be then explained by the Hall-Petch law. It was reported [17] that lower heat input (0.27 kJ/mm) resulted in smaller grain after directed energy deposition, and thus improved the longitudinal tensile strength, almost equal to that of the base metal.

According to [1], there are three reasons for residual stress in the directed energy as-deposited metal, such as spatial temperature gradients (i), thermal expansion and contraction (ii), and plasticity and flow stress (iii). It was found also that the residual stress maximums were on the fusion lines between successively deposited layers as well an absolute maximum was located on the first fusion line between the first layer and a substrate [14].

The residual tensile strain levels measured in as-deposited metal along the building direction proved minimum only for sample 3 obtained at 0.225 kJ/mm. One may suggest that since minimum heat input corresponded to the minimum residual tensile strain then thermal expansion-contraction processes are responsible for inducing the residual strain.

The residual strain distribution along the building direction in sample 2 showed that the maximum strain was found for the first fusion zone between as-deposited metal and the substrate. TEM shows the presence of plastic deformation by twinning and dislocation glide in this zone. This zone showed the minimum tensile strength 492 MPa as compared to those of as-deposited metal 557 MPa and the base metal 539 MPa (Table 1). High tensile stress level as well as work-hardening together with coarse grain structure formed in this zone may explain that low strength.

Deformation twinning in a laser powder-bed AM obtained 316 L austenitic stainless steel was observed and twinning-induced plasticity was claimed responsible for the high strength level achieved [18]. However, in our case, the stress-strain curves did not show any features that could result from twinning-induced plasticity. The twinning resulted from plastic deformation under residual stress exerted due to thermal expansion-contraction conditions. The maximum tensile residual stress was achieved on the first fusion boundary zone, and this zone showed the minimum tensile strength without any twinning-induced plasticity. Also, no one of the stress-strain curves showed a feature that could be related to twinning-induced plasticity. We believe that deformation twinning is inherent with the stainless steels, and there is no surprise observing it.

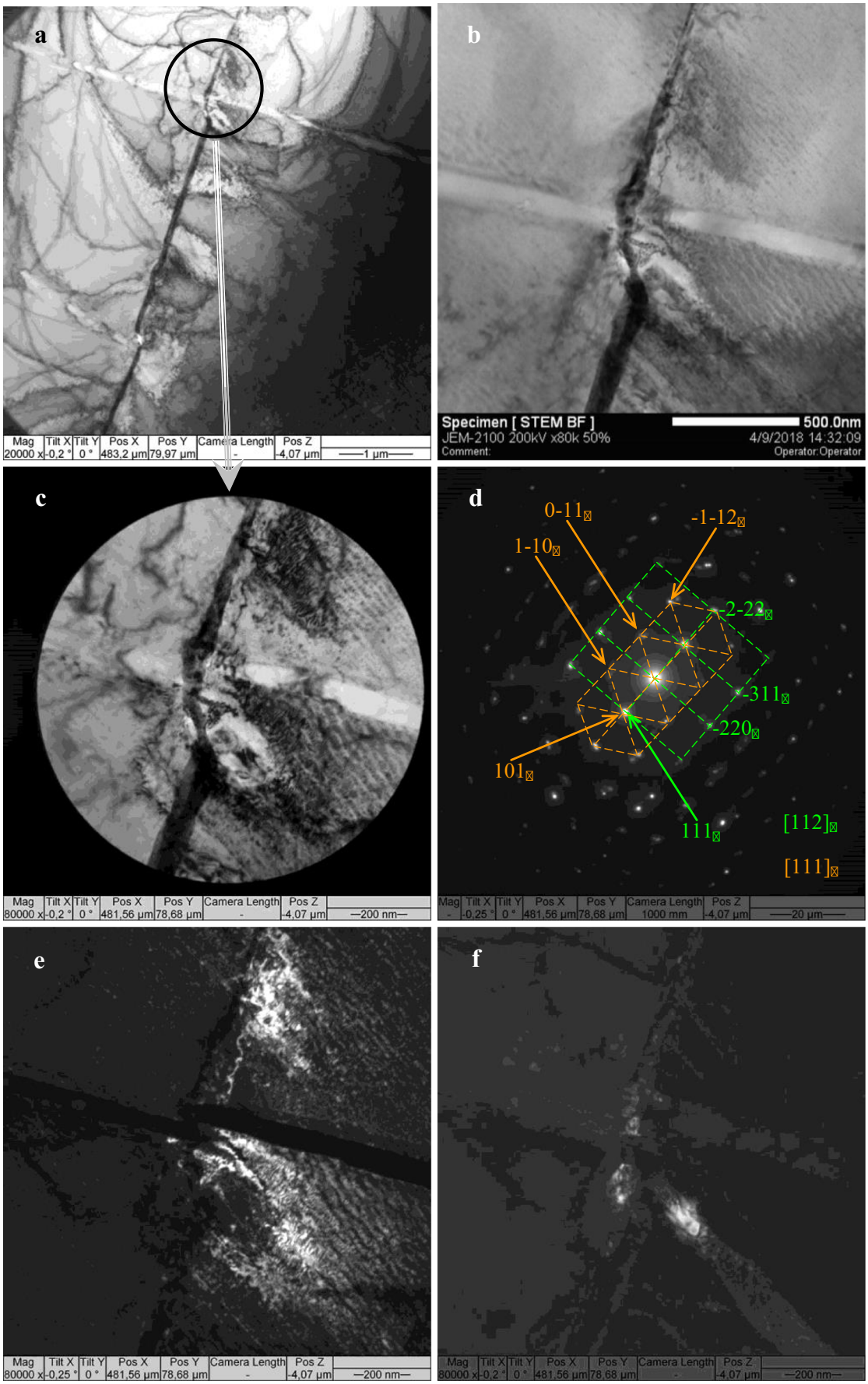
a
Mag 20000 x
Tilt X -0,2 °
Tilt Y 0 °
Pos X 483,2 µm
Pos Y 79,97 µm
Camera Length -
Pos Z -4,07 µm
1 µm
b
Specimen [STEM BF]
JEM-2100 200kV x80k 50%
Comment:
500.0nm
4/9/2018 14:32:09
Operator:Operator
c
Mag 80000 x
Tilt X -0,2 °
Tilt Y 0 °
Pos X 481,56 µm
Pos Y 78,68 µm
Camera Length -
Pos Z -4,07 µm
200 nm
d
0-11
-1-12
1-10
-2-22
-311
-220
101
111
[112]
[111]
Mag -
Tilt X -0,25 °
Tilt Y 0 °
Pos X 481,56 µm
Pos Y 78,68 µm
Camera Length 1000 mm
Pos Z -4,07 µm
20 µm
e
Mag 80000 x
Tilt X -0,25 °
Tilt Y 0 °
Pos X 481,56 µm
Pos Y 78,68 µm
Camera Length -
Pos Z -4,07 µm
200 nm
f
Mag 80000 x
Tilt X -0,2 °
Tilt Y 0 °
Pos X 481,56 µm
Pos Y 78,68 µm
Camera Length -
Pos Z -4,07 µm
200 nm

◀ **Fig. 13** TEM bright-field images of ferrite between austenite dendrites (**a**, **b**, **c**), corresponding SAED pattern (**d**), and dark-field images obtained in reflections $(111)_\gamma$&$(101)_\alpha$ (**e**), $(0\bar{1}1)_\alpha$ (**f**)

5 Conclusion

The results of investigations into electron beam deposited multilayer multipass allowed establishing that the as-deposited metal strength as well as phase composition is determined by heat input level. It was found that an optimal heat input level must be found to provide the highest strength and ferrite content. The insufficient heat input serves to increase the austenite lattice parameter and reduce the ferrite content. On the other hand, the excess heat input may lead to dissolution of ferrite crystallite in the austenite matrix and coarsening of the austenite dendrites. The maximum residual tensile strain and minimum tensile strength zone was found on the first fusion line as well as deformation twinning and dislocation structures formed by thermal expansion-contraction mechanism.

Funding This work was financially supported by the Russian Federation Ministry of Education and Science (agreement no 14.610.21.0013, project identifier RFMEFI61017X0013).

References

1. DebRoy T, Wei HL, Zuback JS, Mukherjee T, Elmer JW, Milewski JO, Beese AM, Wilson-Heid A, De A, Zhang W (2018) Additive manufacturing of metallic components – process, structure and properties. Prog Mater Sci 92:112–224
2. Fuchs J, Schneider C, Enzinger N (2018) Wire-based additive manufacturing using an electron beam as heat source. Welding World. https://doi.org/10.1007/s40194-017-0537-7
3. Taminger KM, Hafley RA (2006) Electron beam freeform fabrication for cost effective near-net shape manufacturing. NATO/RTOAVT-139, Amsterdam
4. Taminger K (2009) Electron beam freeform fabrication. Adv Mater Process 167:45
5. Gockel J, Beuth J, Taminger KM (2014) Integrated control of solidification microstructure and melt pool dimensions in electron beam wire feed additive manufacturing of Ti-6Al-4V. Addit Manuf 1-4:119–126
6. Baufeld B, Widdison R, Dutilleul T, Bridger K (2016) Electron beam additive manufacturing at the nuclear AMRC. Elektronika ir Elektrotechnika 51:25–30
7. Kovalchuk D, Melnyk V, Melnyk I, Tugai B (2016) Prospects of application of gas-discharge electron beam guns in additive manufacturing. Elektronika ir Elektrotechnika 51:36–42
8. Baufeld B, Widdison R, Dutilleul T (2017) Wire based electron beam additive manufacturing, 70th IIW assembly and international conference Shanghai, China
9. Węglowski MS, Błacha S, Pilarczyk J, Dutkiewicz J, Rogal Ł (2018) Electron beam additive manufacturing with wire - analysis of the process. AIP Conf Proc 1960:140015
10. Fuchs J, Schneider C, Enzinger N (2018) Wire-based additive manufacturing using an electron beam as heat source. Welding World 62:267–275
11. Ding D, Pan Z, Cuiuri D, Li H (2015) Wire-feed additive manufacturing of metal components: technologies, developments and future interests. J Adv Manuf Technol 81:465–481. https://doi.org/10.1007/s00170-015-7077-3
12. Inoue H, Koseki T, Ohkita S, Fuji M (2000) Formation mechanisms of vermicular and lacy ferrite in austenitic stainless steel weld metals. Sci Technol Weld Join 5(6):385–396
13. Degterev AS, Gnyusov SF, Tarasov SY (2017) Structural modification in a re-heated bead-overlapping zone of the multiple-pass plasma-transferred arc Fe-Cr-V-Mo-C coating. Surf Coat Technol 329:272–280
14. Yadroitsev I, Yadroitsava I (2015) Evaluation of residual stress in stainless steel 316L and Ti6Al4V samples produced by selective laser melting. Virtual Phys Prototyp 2:67–76. @@https://doi.org/10.1080/17452759.2015.1026045
15. Gnyusov SF, Ignatov AA, Durakov VG, Tarasov SY (2012) The effect of thermal cycling by electron-beam surfacing on structure and wear resistance of deposited M2 steel. Appl Surf Sci 263:215–222
16. Unnikrishnan R, Satish Idury KSN, Ismail TP, Bhadauri A, Shekhawat SK, Khatirkar RK, Sapate SG (2014) Effect of heat input on the microstructure, residual stresses and corrosion resistance of 304L austenitic stainless steel weldments. Mater Charact 93:10–23. https://doi.org/10.1016/j.matchar.2014.03.013
17. Wang Z, Palmer TA, Beese AM (2016) Effect of processing parameters on microstructure and tensile properties of austenitic stainless steel 304L made by directed energy deposition additive manufacturing. Acta Mater 110:226–235. https://doi.org/10.1007/s00170-015-7077-3
18. Phama MS, Dovgyy B, Hooper PA (2017) Twinning induced plasticity in austenitic stainless steel 316L made by additive manufacturing. Mater Sci Eng A 704:102–111